SUPER AWESOME MARATHON THESIS

A dissertation submitted

to Kent State University

in partial fulfillment of the requirements

for the degree of Doctor of Philosophy

by

Tyler Hague

December 2019

Dissertation written by

Tyler Hague

B.S., Abilene Christian University, 2012

Ph.D., Kent State University, TBD

Approved by

<u>Gerassimos Petratos</u>, Co-Chair, Doctoral Dissertation Committee

<u>Assimoula Katramatou</u>, Co-Chair, Doctoral Dissertation Committee

<u>James Doe</u>, Members, Doctoral Dissertation Committee

<u>Julia Doe</u>

<u>Jeffrey Doe</u>

Accepted by

<u>James T. Gleeson</u>, Chair, Department of Physics

<u>James L. Blank</u>, Dean, College of Arts and Sciences

TABLE OF CONTENTS

LIST OF FIGURES

LIST OF TABLES

CHAPTER 1

Electron Scattering and Nuclear Structure

1.1 History

Ernest Rutherford performed what is often considered the first scattering experiment. This experiment fired an α-particle beam at gold foil. The result of this experiment saw most particles pass through the foil completely undeflected. Those that did deflect were scattered at a large range of angles. This gave the world a new view of the nucleus, that of a largely empty space with a few hard scattering centers. We now know that these scattering centers are the nucleus of the atom, formed by a dense combination of protons and neutrons.[1]

Since this time, many experiments have been conducted that expanded our view of the nucleus. The evidence of quarks at SLAC once again revolutionized our understanding of the nucleus. In this experiment, electrons were scattered off protons over a large momentum transfer, q^2, and final hadronic invariant mass, W, range. This experiment noted a "surprisingly weak" q^2 dependence once the kinematics reached the $W > 2\text{GeV}$ range, a key feature of Deep Inelastic Scattering.[2] In this view the nucleons, protons and neutrons, are comprised of quarks. These quarks are elementary particles that define the characteristics and structure of the nucleon.[3]

This discovery paved the way for a wave of Deep Inelastic Scattering experiments. These experiments have refined our understanding of the nucleus and its constituent components. Deep Inelastic Scattering has proven to be a one of the most powerful tools available when one seeks to study nuclear structure.

1.2 Electron Scattering

Electron scattering allows for finely tuned analysis of the nucleus. By manipulating the energy of the incoming electron and the kinematic variables accepted by the detectors used, experimenters can choose what aspect of the nucleus will be probed. This technique has been used to study the structure of the nucleus all the way down to the properties of the constituent quarks.

There are four kinematic regimes of electron scattering that can be explored: elastic, quasi-elastic, resonance, and deep inelastic scattering. Each of these regimes are defined by the kinematics and the underlying physical structure that they are sensitive to.

Elastic scattering occurs when the electron scatters coherently off of the nucleus. This occurs at low momentum and energy transfer. At these kinematics, the electron is sensitive to the size of the nucleus. The size of the nucleus is accessed by extracting nuclear "form factors" from the measured cross sections. From this we can learn about the charge distributions, magnetic moments, and charge radius of the nucleus.

Quasi-elastic scattering occurs at larger energy transfers when the electron scatters elastically off of the nucleon, rather than the nucleus. At these kinematics, the electron is sensitive to the form factors of the nucleon.

Resonance scattering occurs at even larger momentum and energy transfers. In this region, some of the energy is used to excite the nucleon into a higher energy state, called a resonance. A resonance is a short-lived particle. The resonance will quickly decay back into the nucleon and emit the excess energy as an additional particle. For example, $ep \rightarrow e\Delta^+ \rightarrow ep\pi^0$.

As we push the momentum and energy transfer further, we enter the Deep Inelastic Scattering (DIS) region. As Q^2 is increased into the transition region between resonance and DIS, the resonance peaks begin to smooth out. Here the electron becomes sensitive to the constituent parts of the nucleon. The wavelength of the exchanged photon is inversely proportional to Q^2. DIS scattering is of particular interest because the wavelength is sufficiently small enough to discern the parton structure. Through careful measurement, we can access the nuclear structure functions and the parton distributions in the the the nucleons.[4–6]

The MARATHON experiment seeks to study the nuclear and nucleon structure functions, as well as nucleon parton distributions. The kinematics used are in the DIS region in order to facilitate this study. The remainder of this chapter will be focused on the DIS cross section and what we can learn from it.

1.2.1 Deep Inelastic Scattering Cross Section

Deep Inelastic Scattering, shown in Figure 1, involves a high energy electron scattering off of a nucleon. In the lowest order perturbation, a virtual photon is exchanged between the electron and
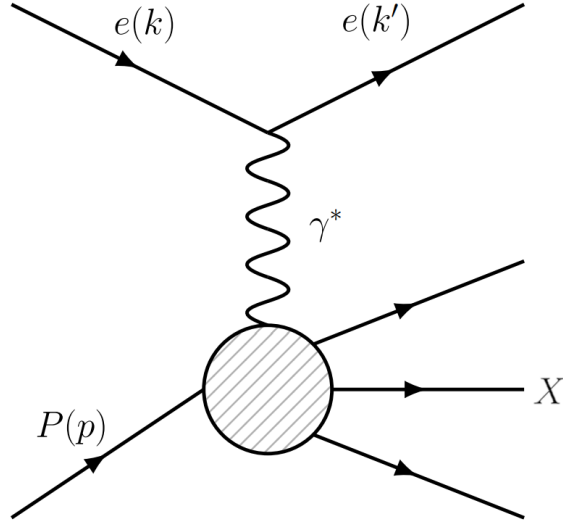
Figure 1: Feynman Diagram of Deep Inelastic Scattering

nucleon. This momentum transfer then excites the nucleon into a hadronic final state. Though the final hadronic state is undetected, the detection of the scattered electron can yield insight into the interaction.

The reaction, for scattering off a proton, is written as:

$$e^- + P \rightarrow e^- + X$$

In this section, there will be many variables defined. For clarity, the meaning of these variable are defined in Table 1. Mathematical definitions will follow as necessary.

The kinematics of scattering are typically defined by he Lorentz-invariant kinematic variables Q^2 and W^2, as well as the energy difference ν. These variables are defined as:

$$q^2 \equiv -Q^2 = \left(k - k'\right)^2 \tag{1.1}$$

$$W^2 = (p + q)^2 \tag{1.2}$$

$$\nu = E - E' \tag{1.3}$$

3

Q^2	Negative of the 4-momentum transfer
W^2	Square of the invariant mass of the final hadronic state
E	Beam energy
E'	Scattered electron energy
$L_{\mu\nu}$	Electron tensor
$W^{\mu\nu}$	Symmetric hadronic tensor
k	4-momentum of the incident electron
k'	4-momentum of the scattered electron
p	4-momentum of the target nucleon
θ	Scattered electron angle
ν	Energy difference between incoming and scattered electron
M	Proton mass
m	Electron mass

Table 1: Variable definitions introduced in this section

Now it is useful to analyze in the laboratory rest frame and to note that MARATHON is a fixed target experiment. In this frame, the target is "at rest" (i.e. having a four-momentum of $(M, 0)$). This leads to a simplification of Q^2 and W^2.

$$Q^2 = 4EE' \sin^2 \frac{\theta}{2} \tag{1.4}$$

$$W^2 = M^2 + 2M\nu - Q^2 \tag{1.5}$$

Electron-nucleon scattering can be generally expressed as the following:

$$\frac{d^2\sigma}{d\Omega dE'} = \frac{\alpha^2}{Q^4} \frac{E'}{E} L_{\mu\nu} W^{\mu\nu} \tag{1.6}$$

The electron tensor is expressed as:

$$L_{\mu\nu} = 2 \left(k'^\mu k^\nu + k'^\nu k^\mu - \left(k' \cdot k - m^2 \right) g^{\mu\nu} \right) \tag{1.7}$$

The DIS hadronic tensor is expressed in terms of structure functions W_1 and W_2:

4

$$W^{\mu\nu} = W_1 \left(-g^{\mu\nu} + \frac{q^\mu q^\nu}{q^2} \right) + \frac{W_2}{M^2} \left(p^\mu - \frac{p \cdot q}{q^2} q^\mu \right) \left(p^\nu - \frac{p \cdot q}{q^2} q^\nu \right) \tag{1.8}$$

Combining all of this, we arrive at the *ep* DIS cross section in the laboratory frame:

$$\left. \frac{d^2\sigma}{d\Omega dE'} \right|_{\text{lab}} = \frac{\alpha^2}{4E^2 \sin^4 \frac{\theta}{2}} \left[W_2 \cos^2 \frac{\theta}{2} + 2W_1 \sin^2 \frac{\theta}{2} \right] \tag{1.9}$$

1.3 Bjorken Scaling

As Q^2 is pushed higher, inelastic scattering begins to give way to DIS. In this kinematic region, the wavelength of the virtual photon is sufficiently short to resolve the internal structure of the nucleon. This transition sees the system begin to behave like a free Dirac particle, the parton. As the Bjorken limit is approached, $Q^2 \to \infty$ and $\nu \to \infty$, the scattering center approaches a structureless parton.[7] With this in mind, it is useful to look at the cross section for scattering off of a structureless target:

$$\frac{d^2\sigma}{d\Omega dE'} = \frac{\alpha^2}{4E^2 \sin^4 \frac{\theta}{2}} \left[\cos^2 \frac{\theta}{2} + \frac{Q^2}{2m^2} \sin^2 \frac{\theta}{2} \right] \delta \left(\nu - \frac{Q^2}{2M} \right) \tag{1.10}$$

Noting that DIS is scattering off of a structureless parton, we can compare (1.9) and (1.10). By equating these two cross sections, we can clearly extract equations for the DIS structure functions.

$$2MW_1 \left(Q^2, \nu \right) = \frac{Q^2}{2M\nu} \delta \left(1 - \frac{Q^2}{2M\nu} \right) \tag{1.11a}$$

$$\nu W_2 \left(Q^2, \nu \right) = \delta \left(1 - \frac{Q^2}{2M\nu} \right) \tag{1.11b}$$

In this kinematic region, we see that the structure functions are dependent on the ratio $\frac{Q^2}{2M\nu}$ rather than Q^2 and ν independently while the target mass sets the scale. Noting this dependency, the scaling variable Bjorken x is defined as

$$x = \frac{Q^2}{2M\nu}. \tag{1.12}$$

As the Bjorken limit is approached DIS is only dependent on x, showing little to no scaling with Q^2 or ν.[8] New structure functions, F_1 and F_2, are also defined in terms of x to clearly show the lack of scaling with Q^2 and ν independently:
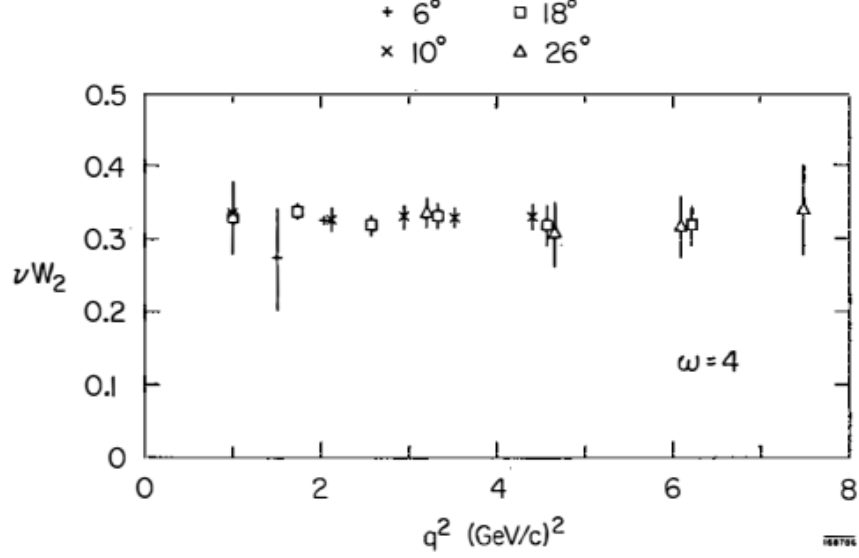
Figure 2: Proton data showing no Q^2 dependence of $\nu W_2 = F_2$ in the DIS region.[9]

$$2MW_1\left(Q^2,\nu\right) \to F_1\left(x\right) \tag{1.13a}$$

$$\nu W_2\left(Q^2,\nu\right) \to F_2\left(x\right) \tag{1.13b}$$

The independence of structure functions with respect to Q^2 has been experimentally tested. The data was taken at fixed x with varying Q^2. All measurements were consistent with no Q^2 dependence. Proton data showing this effect for the structure function F_2 can be seen in Figure 2. Substituting Equations 1.13 into Equation 1.9 we find the cross section in terms of DIS x, Equation 1.14.

$$\frac{d^2\sigma}{d\Omega dE'} = \frac{4\alpha^2\left(E'\right)^2}{Q^4}\cos^2\left(\frac{\theta}{2}\right)\left[\frac{F_2\left(x\right)}{\nu} + \frac{2F_1\left(x\right)}{M}\tan^2\left(\frac{\theta}{2}\right)\right] \tag{1.14}$$

1.4 Nuclear Structure Functions and The Quark Parton Model

Having shown that the nucleons consist of structureless partons we can define physics quantities in terms of the Quark-Parton Model (QPM). The QPM defines kinematic properties of the quarks and the nucleon structure functions in terms of constituent quark properties in the Bjorken limit.

In this regime, Bjorken x is the fraction of the momentum and energy contained by the parton scattered off of. To access the kinematics of the parton, we simply multiply the energy, momentum, and mass of the nucleon by x.

To analyze the structure functions of the nucleon, we first look at elastic scattering off of a parton. In this setup, we imagine that we have the means to determine what parton type the electron was scattered from. This is the same equation as Equation 1.10, but with α multiplied by the charge of the parton being scattered from, e_i, and replacing M with xM for the mass of the parton.

$$\frac{d^2\sigma}{d\Omega dE'} = \frac{\alpha^2 e_i^2}{4E^2 \sin^4 \frac{\theta}{2}} \left[\cos^2 \frac{\theta}{2} + \frac{Q^2}{2x^2 M^2} \sin^2 \frac{\theta}{2}\right] \delta\left(\nu - \frac{Q^2}{2xM}\right) \tag{1.15}$$

Comparing this with the nuclear inelastic cross section, it is clear that the nuclear structure functions can be written in terms of parton structure functions. The parton structure functions can be derived using the same method as the nuclear structure functions.

$$W_1^i = \frac{e_i^2 Q^2}{4M^2 x^2 \nu} \delta\left(1 - \frac{Q^2}{2Mx\nu}\right) \tag{1.16a}$$

$$W_2^i = \frac{e_i^2}{\nu} \delta\left(1 - \frac{Q^2}{2Mx\nu}\right) \tag{1.16b}$$

Defining $f_i(x)$ as the probability that a parton i has the momentum fraction x, or parton distribution, we can then write the nucleon structure functions in terms of the parton structure functions. The delta function makes the integrals trivial.

$$W_1\left(Q^2, \nu\right) = \sum_i \int_0^1 \frac{e_i^2 Q^2}{4M^2 x^2 \nu} f_i(x) \delta\left(1 - \frac{Q^2}{2Mx\nu}\right) dx = \sum_i \frac{e_i^2}{2M} f_i(x) \tag{1.17a}$$

$$W_2\left(Q^2, \nu\right) = \sum_i \int_0^1 \frac{e_i^2}{\nu} f_i(x) \delta\left(1 - \frac{Q^2}{2Mx\nu}\right) dx = \sum_i \frac{e_i^2}{\nu} f_i(x) \tag{1.17b}$$

Using the definitions of the F structure functions in the previous sections, this formalism allows us to write them in terms of parton quantities.

$$MW_1\left(Q^2, \nu\right) = \sum_i \frac{e_i^2}{2} f_i(x) \equiv F_1(x) \tag{1.18a}$$

$$\nu W_2\left(Q^2, \nu\right) = \sum_i e_i^2 x f_i(x) \equiv F_2(x) \tag{1.18b}$$

7

These equations lead to a relation between the structure functions (in the Bjorken limit) called the Callan-Gross relation:

$$F_2(x) = 2xF_1(x) \tag{1.19}$$

Deriving the structure functions in terms of parton quantities also allows us to place constraints on the ratio of F_2 for the nucleons. Due to mass constraints, we can restrict this analysis to up ($q = 2/3$), down ($q = -1/3$), and strange ($q = -1/3$) quarks. Since the proton and neutron, along with the up and down quarks, form an isospin doublet we can relate their quark distributions (and extend this to their antiquark distributions):

$$u^p(x) = d^n(x) \equiv u \tag{1.20a}$$

$$d^p(x) = u^n(x) \equiv d \tag{1.20b}$$

$$s^p(x) = s^n(x) \equiv s \tag{1.20c}$$

Using these relations, we can write the nucleon structure functions and their ratio as:

$$F_2^p = x\left[\frac{4}{9}(u + \bar{u}) + \frac{1}{9}(d + \bar{d}) + \frac{1}{9}(s + \bar{s})\right] \tag{1.21a}$$

$$F_2^n = x\left[\frac{4}{9}(d + \bar{d}) + \frac{1}{9}(u + \bar{u}) + \frac{1}{9}(s + \bar{s})\right] \tag{1.21b}$$

$$\frac{F_2^n}{F_2^p} = \frac{[(u + \bar{u}) + (s + \bar{s})] + 4(d + \bar{d})}{[(d + \bar{d}) + (s + \bar{s})] + 4(u + \bar{u})} \tag{1.22}$$

This equation can be evaluated noting that by definition quark distributions must be positive. This naturally leads to a constraint on F_2^n/F_2^p known as the Nachtmann inequality:

$$\frac{1}{4} \leq \frac{F_2^n}{F_2^p} \leq 4 \tag{1.23}$$

1.5 $R = \sigma_L/\sigma_T$

If we instead approach DIS as the production and absorption of a virtual photon by a parton we can extract a different structure function $R = \sigma_L/\sigma_T$, referred to as photonuclear R. That is, the ratio of the cross sections for absorbing longitudinal photons, σ_L, to transverse photons, σ_T. In

8

the Bjorken limit, as in the previous section, $R \to 0$. In practice the Bjorken limit is an imperfect approximation and it is useful to consider the effects of large, but finite, Q^2 and ν.

We can write the DIS cross section in terms of these cross sections as

$$\frac{d^2\sigma}{d\Omega dE'} \left(E, E', \theta\right) = \Gamma \left[\sigma_T \left(x, Q^2\right) + \epsilon \sigma_L \left(x, Q^2\right)\right]. \tag{1.24}$$

In this equation Γ is the flux of transverse virtual photons and ϵ is the relative flux of longitudinal virtual photons. These are defined by

$$\Gamma = \frac{\alpha K E'}{2\pi^2 Q^2 E_0 \left(1 - \epsilon\right)} \tag{1.25}$$

and

$$\epsilon = \frac{1}{1 + 2 \left(1 + \nu^2/Q^2\right) \tan^2\left(\frac{\theta}{2}\right)}. \tag{1.26}$$

Here, K is the laboratory photon energy,

$$K = \frac{W^2 - M^2}{2M}. \tag{1.27}$$

By comparing these equations to Equation 1.14 F_1 and F_2 can be related to σ_L, σ_T, and each other.

$$\sigma_T = \frac{4\pi\alpha^2}{KM} F_1 \tag{1.28}$$

$$\sigma_L = \frac{4\pi\alpha^2}{KM} \frac{1}{2x} \left[F_2 - 2xF_1\right] \tag{1.29}$$

$$F_1 = \frac{F_2 \left(1 + Q^2/\nu^2\right)}{2x \left(1 + R\right)} \tag{1.30}$$

Substituting this into our DIS cross section equation, we can eliminate F_1. This also makes it clear that we can easily access the F_2 structure functions by measuring cross section ratios.

$$\frac{d^2\sigma}{d\Omega dE'} \left(E, E', \theta\right) = \frac{4\alpha^2 \left(E'\right)}{Q^4} \cos^2\left(\frac{\theta}{2}\right) F_2 \left[\frac{1}{\nu} + \frac{\left(1 + Q^2/\nu^2\right)}{xM \left(1 + R\right)} \tan^2\left(\frac{\theta}{2}\right)\right] \tag{1.31}$$

If we measure the cross section ratios of two different targets at the same kinematics (that is the same x, E, E', and θ) we find:

	Nuclei	X	Q^2
SLAC	Au-D	.20	5.0
SLAC	Fe-D	.50	5.0
SLAC	Fe-D	.50	2.5
SLAC	Fe-D	.50	2.5
SLAC	Fe-D	.35	5.0
SLAC	Fe-D	.35	2.5
SLAC	Fe-D	.35	1.0
SLAC	Fe-D	.20	2.5
SLAC	Fe-D	.20	1.5
SLAC	Fe-D	.20	1.0
SLAC	Fe-D	.20	1.0
NMC	Ca-C	.15	5.3
NMC	Ca-C	.08	3.3
NMC	Ca-C	.05	2.6
NMC	Ca-C	.03	2.1
NMC	Ca-C	.015	1.4
NMC	Ca-C	.008	0.9
SLAC	D-H	.660	17.6
SLAC	D-H	.775	11.7
SLAC	D-H	.700	9.6
SLAC	D-H	.625	8.7
SLAC	D-H	.550	8.0
SLAC	D-H	.475	6.2
SLAC	D-H	.400	5.3
SLAC	D-H	.325	3.9
SLAC	D-H	.250	2.5
SLAC	D-H	.175	1.9
SLAC	D-H	.100	1.5
NMC	D-H	.25	15.2
NMC	D-H	.175	12.3
NMC	D-H	.125	10.0
NMC	D-H	.08	7.7
NMC	D-H	.05	5.9
NMC	D-H	.03	4.2
NMC	D-H	.015	2.6

Figure 3: Historical data of $R = \sigma_L/\sigma_T$. This data shows measurements of the difference in R between two nuclei. The data is consistent with no nuclear dependence.[10]

$$\frac{\sigma_A}{\sigma_B} = \frac{F_2^A}{F_2^B} \frac{\left[\frac{1}{\nu} + \frac{\left(1+Q^2/\nu^2\right)}{xM(1+R^A)} \tan^2\left(\frac{\theta}{2}\right)\right]}{\left[\frac{1}{\nu} + \frac{\left(1+Q^2/\nu^2\right)}{xM(1+R^B)} \tan^2\left(\frac{\theta}{2}\right)\right]} \tag{1.32}$$

As shown in Figure 3, historical data suggests that photonuclear R has no nuclear dependence to within 10%. If we assume that that there is no nuclear dependence, this equation simplifies to:

$$\frac{\sigma_A}{\sigma_B} = \frac{F_2^A}{F_2^B} \tag{1.33}$$

By measuring the cross section ratios of targets in the DIS region, we can easily access the nuclear structure functions of the targets.

1.6 F_2^n/F_2^p

The structure functions of the nucleons are common inputs to models. Making use of a Hydrogen target the F_2^p structure function is easily accessible. Unfortunately, there is no free neutron target. This absence means that there is no way to direct way to measure F_2^n. However, with the proper input, we can extract the ratio F_2^n/F_2^p.

To extract this ratio, we first define "EMC-type" ratios. These are simply the ratio of the nuclear structure function to the sum of its constituent nucleons. The "EMC-type" ratios for ^{3}He and ^{2}H are:

$$R_{\text{EMC}}\left(^3\text{He}\right) = \frac{F_2^{^3\text{He}}}{2F_2^p + F_2^n} \tag{1.34}$$

$$R_{\text{EMC}}\left(^2\text{H}\right) = \frac{F_2^{^2\text{H}}}{F_2^p + F_2^n} \tag{1.35}$$

These can be used to create a "Super-Ratio", $\mathcal{R}$, as the ratio of "EMC-type" ratios.

$$\mathcal{R} = \frac{R_{\text{EMC}}\left(^3\text{He}\right)}{R_{\text{EMC}}\left(^2\text{H}\right)} = \frac{F_2^{^3\text{He}}}{2F_2^p + F_2^n} \cdot \frac{F_2^p + F_2^n}{F_2^{^2\text{H}}} \tag{1.36}$$

Solving this for F_2^n/F_2^p makes it clear that the quantity can be easily extracted with a cross section ratio measurement and a model input for $\mathcal{R}$.

$$\frac{F_2^n}{F_2^p} = \frac{F_2^{^3\text{He}}/F_2^{^2\text{H}} - 2\mathcal{R}}{\mathcal{R} - F_2^{^3\text{He}}/F_2^{^2\text{H}}} \tag{1.37}$$

CHAPTER 2

The EMC Effect

2.1 History

The EMC effect was first discovered by its namesake the European Muon Collaboration (EMC group) in 1983. The EMC group measured the structure functions of hydrogen, deuterium, and iron. After correcting for the neutron excess, the per nucleon F_2 structure function ratio of iron to deuterium was calculated, as seen in Figure 4. This data showed a clear x dependence, contrary to expectations.

Prior to this original measurement, nucleons were assumed to be quasi-free within the nucleus. In this understanding the nuclear F_2 structure function would be described as

$$F_2^A = Z F_2^p + (A - Z) F_2^n. \tag{2.1}$$

This description leads to the prediction that the per nucleon structure function ratio of any two isoscalar targets will be unity. At this time, the only other expected nuclear effect was Fermi motion. Fermi motion causes a sharp rise in the per nucleon structure function ratio at high x, but would leave the ratio largely unchanged at low x.

The original experiment did not originally set out to measure the EMC effect, rather the data was a byproduct of efforts to achieve higher luminosity. Because of this, the data had very large uncertainty on the measurement. However, the uncertainties were small enough that the anomaly could be confirmed.

Shortly after the original EMC measurement a Rochester-SLAC-MIT group analyzed previous SLAC data to confirm the phenomenon. The data analyzed not only confirmed the effect in iron, but also in aluminum. The iron data showed the EMC effect as well as the expected rise from Fermi motion at high x. The aluminum data showed these phenomena as well as low x shadowing and anti-shadowing. [12–14]
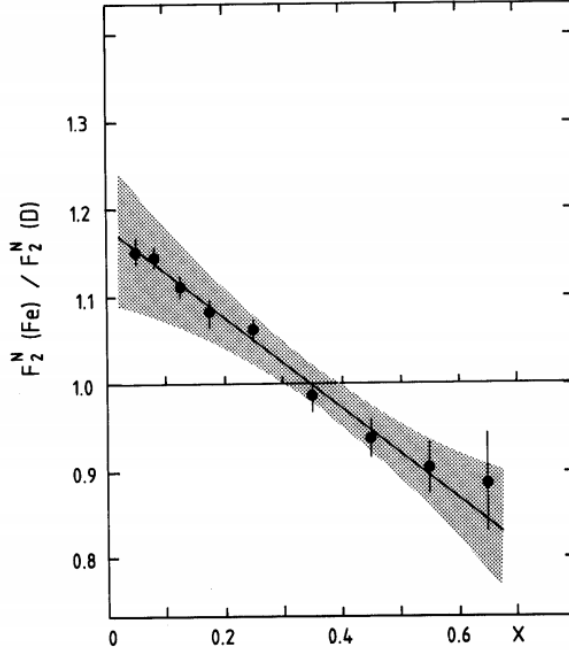
Figure 4: Results from the EMC collaboration showing a clear x dependence of the per-nucleon F_2 structure function ratio[11]

2.2 Further Results

Since that time, numerous experiments have measured nuclear F_2 structure function data in order to better understand the nature of this anomaly. These searches have primarily focused on heavy isoscalar nuclei. The following represents a non-exhaustive presentation of these experiments.

2.2.1 SLAC

At SLAC a new experiment was set up with the explicit goal of measuring the EMC effect in a wide range of nuclei. The data cover a large kinematic range of $0.089 \leq x \leq 0.8$ and $2 \, (\text{GeV/c})^2 \leq Q^2 \leq 15 \, (\text{GeV/c})^2$. This data confirms the phenomenon seen by the EMC group in the $x > 0.3$ region, but also sees a downturn in the ratios at low x.

The targets studied were ^{4}He, Be, C, Al, Ca, Fe, Ag, and Au. These results are shown in Figure 5. This target range allowed them to study the mass number A-dependence of the EMC effect. This data suggests an approximately $\ln(A)$ dependence on the strength of the EMC effect, with notable outliers of ^{4}He and Be. [15, 16]
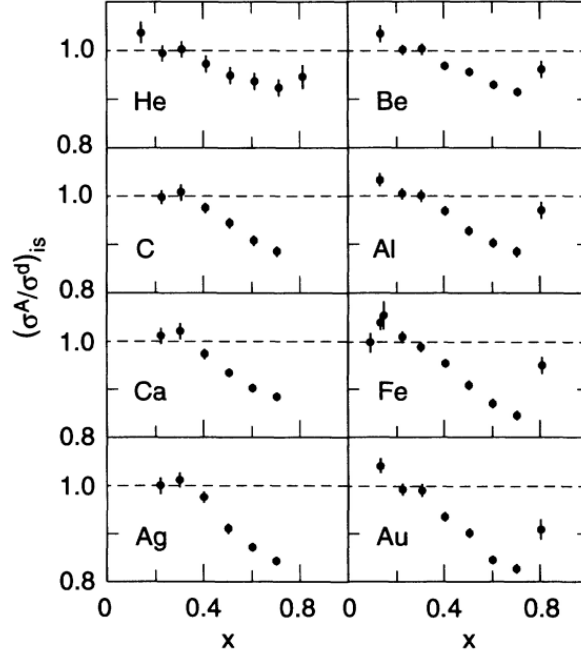
Figure 5: Results from SLAC showing an A-dependent EMC effect[16]

2.2.2 BCDMS

The BCDMS experiment at CERN measured the N and Fe EMC ratios. The iron data is consistent with the original EMC measurement within a normalization discrepancy. The nitrogen data is consistent with the SLAC carbon data. The BCDMS results show no Q^2 dependence in the EMC effect. However, BCDMS does not demonstrate an A-dependence of the EMC effect as SLAC did.[14]

2.2.3 EMC

The EMC group performed three more experiments to study the EMC effect.

The first of these experiments set out to improve the systematics of the original experiment. This followup measured the EMC ratio of C, Cu, and Sn. This data agrees with the original data for $x \geq 0.08$. However, below this threshold the data sees a downturn, the shadowing region, that the original experiment did not see.[17]

The NA28 experiment focused on studying the EMC ratio of C and Ca at low x. This data confirms the shadowing effect seen in the previous EMC data, the ratio drops below unity in the

region of $x < 0.1$. These results also shows that the shadowing region has no Q^2 dependence. The data overlaps well with previous measurements.

The last EMC group experiment to study the EMC effect remeasured the copper EMC ratio. To minimize systematics two 1m ^{2}H targets and three Cu targets were used. These results agree with the results from the first followup and are of greater precision.

2.2.4 NMC

The New Muon Collaboration (NMC) continued the study of the EMC effect at CERN. Initially NMC measure the EMC ratio of Li, C, and Ca to high precision at low x. This data was taken with two goals: to confirm the EMC data in the shadowing region and to study the effect of nuclear size and density on the EMC ratio. The data confirms the previous EMC measurement and found a very weak Q^2 dependence. Lithium and carbon have approximately the same size nucleus, but different nuclear densities. Calcium and carbon have the approximately the same nuclear density, but calcium has a bigger nucleus. It was found that both of these factors play a part in the suppression of the EMC ratio in the shadowing region. Increases in nuclear size or density show an increase in the suppression of the EMC ratio due to nuclear shadowing.

NMC then set out to study the difference between the photonuclear R of different targets in the region of $0.01 \leq x \leq 0.3$. The results were found, within uncertainties, to be compatible with zero. This result confirms that $\sigma_A/\sigma_D = F_2^A/F_2^D$.

Finally, the NMC group studied the EMC effect on Be, C, Al, Ca, Fe, Sn, and Pb. These results again confirm that there is no Q^2 dependence of the EMC ratio above $x = 0.06$. These data agree with the SLAC result finding that the EMC effect is approximately logarithmic with A.[18]

2.2.5 HERMES

The HERMES experiment ran at the HERA collider. This experiment collided positrons with protons to study the EMC effect on ^{3}He and N. Data was taken for $0.013 \leq x \leq 0.65$ and $0.5\,(\mathrm{GeV/c})^2 \leq Q^2 \leq 15\,(\mathrm{GeV/c})^2$. In the $x < 0.06$ region, the HERMES results differed drastically from the NMC results. Initially this was misreported as an A dependence of photonuclear R. This reporting was later amended when it was found that the difference could be attributed to a previously unaccounted for systematic effect.
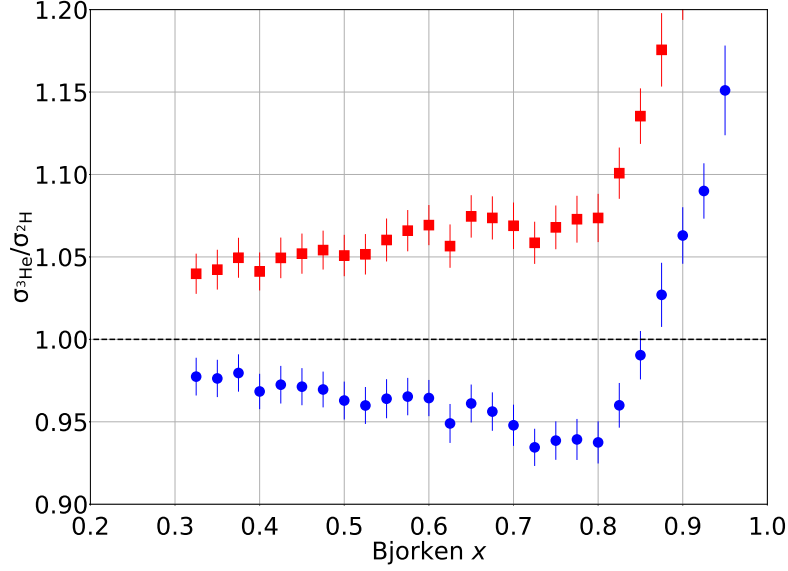
Figure 6: Helium-3 results from JLab E03-103. The upper red squares are the raw ratio and the lower blue circles have an isoscalar correction applied.[19]

2.2.6 JLab

The E03-103 experiment ran in Hall C at Jefferson Lab. This experiment studied the EMC effect in ^{3}He, ^{4}He, Be, and C. The kinematics covered were $0.3 < x < 0.9$ and $3\,(\mathrm{GeV/c})^2 < Q^2 < 6\,(\mathrm{GeV/c})^2$. The data measured was not purely DIS, but also included data in the resonance region. This led the experiment to extensively verify that their data was indeed independent of Q^2. The data for Beryllium is noted not to match the previous SLAC data. This is caused by the use of a different isoscalar correction and is further rectified by noting normalization uncertainties. These data show a significantly larger EMC effect in Beryllium than expected by the $\ln(A)$ prediction, which is consistent with SLAC noting that Beryllium is an outlier. The suggested explanation is that the EMC effect is dependent on *local* nuclear density rather than mean nuclear density. The ^{3}He results are showing in Figure 6.[19]

2.3 Structure Regions

In DIS F_2 structure function data, there are four phenomenological regions. In each region, different physics dominates the shape of the structure function ratio. Each kinematic region provides is a test bed for our understanding of nuclear physics. Studying these nuclear effects is the driving force

16

behind many experiments.[20, 21]

2.3.1 Shadowing

Nuclear shadowing is a phenomenon that occurs in the region of $x < 0.1$. Here, there is a depletion of the structure function when compared to deuterium. This depletion increases with mass number A. This depletion is also weakly dependent on Q^2 and mass number A. This effect is typically explained in terms of nuclear scattering which can be further investigated in reference [22].

2.3.2 Anti-shadowing

The Anti-shadowing, or enhancement, region is from $0.1 \leq x \leq 0.3$. In this region, the EMC structure function ratios are enhanced to greater than 1. Within experimental uncertainties, there is no Q^2 dependence in the anti-shadowing region.

2.3.3 EMC Effect

The EMC Effect region spans from $0.3 \leq x \leq 0.8$. In this kinematic area, the EMC structure function ratio falls off and reaches a minimum around $x = 0.65$. Since the discovery of the effect by the European Muon Collaboration, extensive EMC Effect region data has been recorded over a large Q^2 range. The data suggests that the EMC Effect is largely independent of Q^2. The EMC Effect does appear to be logarithmically dependent on mass number A.

2.3.4 Fermi Motion

As x is pushed past 0.8 the EMC structure function ratio sharply increases far beyond unity. In this region it is known that F_2^N, the free nucleon structure function, to drop as $(1-x)^3$. Fermi motion increases the structure function of the bound nucleon, causing the ratio to show this sharp increase.

2.4 Theories

There are many theories as to the origin of the EMC effect. To cover them all is beyond the scope of this thesis. This section will discuss the broad classes of models which can be investigated further in [10, 14, 23].

There are two primary groups of theories. Nuclear Structure focuses on the physics of scattering from a nucleus. Nucleon modification focuses on changes to quark momenta due to confinement effects.

2.4.1 Nuclear Structure

Nucleon Models

Traditional scattering calculations assume that the scattered nucleon was on-shell. This class of models gives the struck nucleon a negative average energy $\langle \epsilon \rangle$. This energy shift causes a rescaling of the x. This rescaling can explain the EMC effect region and Fermi motion. However, it is not capable of reproducing the anti-shadowing region.

Pion Enhancement

An enhancement of the nuclear pion field by nucleon-nucleon interactions. In these models the pion contribution is concentrated to low x. The creation of pions also requires the creation of Δ resonances in the nucleus.

Alone, this class of model has several problems. To reproduce high x data requires the presence of significantly more Δs than calculations suggest are plausible. In addition to this, matching anti-shadowing data causes a mismatch in high x data.

2.4.2 Nucleon Modification

Quark Bags

In quark cluster models quarks are confined to "bags" as defined by the MIT bag model. This creates color-singlet states with multiples of 3 quarks. The most common quark bag models rely on 6-quark bags. 6-quark bags are larger than a nucleon and thus lead to partial deconfinement of the quarks. This increase in confinement size leads to a decrease in quark momenta due to the uncertainty principle. A decrease in quark momenta in this way will suppress the structure function in the EMC region, leading to the EMC effect. [14, 23]

This quark bag model alone can compute many nuclear affects. It is hampered by the need for an additional free parameter to compute each new observable. This model has fallen out of favor due to failed predictions in the nuclear Drell-Yan process. [23]

Mean Field Enhancement

Mean Field Enhancement suggests that the structure functions of the nucleons are modified by nucleus surrounding them. Nucleons confined within the nucleus exchange mesons between the quarks of other confined nucleons. This modifies the nucleons structure to change the size of the quark confinement. The predicted increase in confinement size yields a smaller quark momentum.

[23, 24]

Short Range Correlations

Short Range Correlations (SRCs) greatly modify a few nucleons, rather than the small modification to all nucleons in mean-field enhancement. SRCs are the idea that there is a probability that two nucleon wavefunctions will overlap. In this scenario the overlapping wavefunctions will cause the size of quark confinement to greatly increase, drastically decreasing the quark momenta.

SRCs also predict an observed high momentum tail at $x > 1$. Studies of this effect have noted a correlation between the SRC "scale factor" and the strength of the EMC effect, the slope of the EMC ratio in the EMC region. [23, 25, 26]

Discerning between Mean Field Enhancement and SRCs

Both Mean Field Enhancement and SRCs have been shown to have accurate predictive power within the datasets available. This leads to the conundrum of finding an unmeasured quantity for which the two models make different predictions. Hen [23] and Thomas [27] discuss that mean field theory and SRCs make seemingly contradictory predictions for the polarized EMC effect. Mean field theory predicts that polarization will enhance the effect; SRCs predict the polarization to minimize the effect. This will be tested in Jefferson Lab Hall C by measuring the spin structure functions of ^{7}Li [28].

CHAPTER 3

The Experimental Setup

3.1 CEBAF Accelerator

The Continuous Electron Beam Accelerator Facility (CEBAF) accelerator is a recirculating accelerator at Thomas Jefferson National Accelerator Facility (JLab). That is, there are two linear accelerators (linacs) connected by recirculation arcs. CEBAF has recently undergone an upgrade which increased the maximum possible energy to 12 GeV (to Hall D). The 12-GeV configuration of CEBAF can be seen in Figure 7. Electrons traveling through both linacs a single time is called a "pass". Halls A, B, and C are capable of receiving up to 5 pass beam; Hall D can receive up to 5.5 pass beam. The beam provided is Continuous Wave (CW), comprised of a steady stream of electrons rather than many electrons in short pulses.
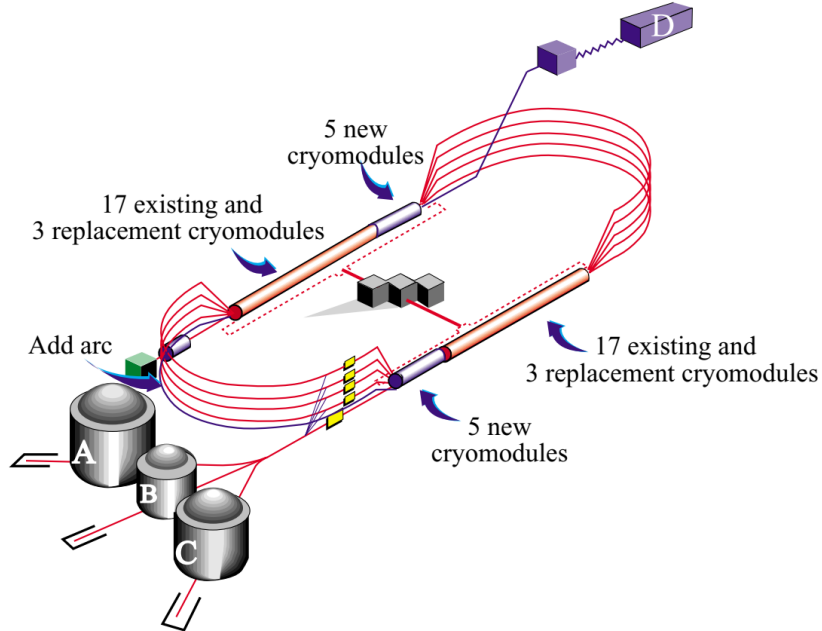

Figure 7: The current 12-GeV configuration of the CEBAF accelerator with the upgrades that were made from the 6-GeV configuration.[29]

3.2 Beamline Components

When the electrons from the CEBAF Accelerator have circulated the desired number of passes, they then enter the Hall A beamline. The Hall A Beamline has several measurement devices that allow the experimenter to fully understand the beam that is being delivered to the hall. A schematic of Hall A with the beamline components that are present in the hall can be seen in Figure 8. High beam quality and understanding the beams characteristics are critical for accurate analysis of an experiment. In the MARATHON experiment, the critical beamline components (which will be described in this section) are:

- Beam Arc Energy Measurement

- Beam Current Monitor

- Raster
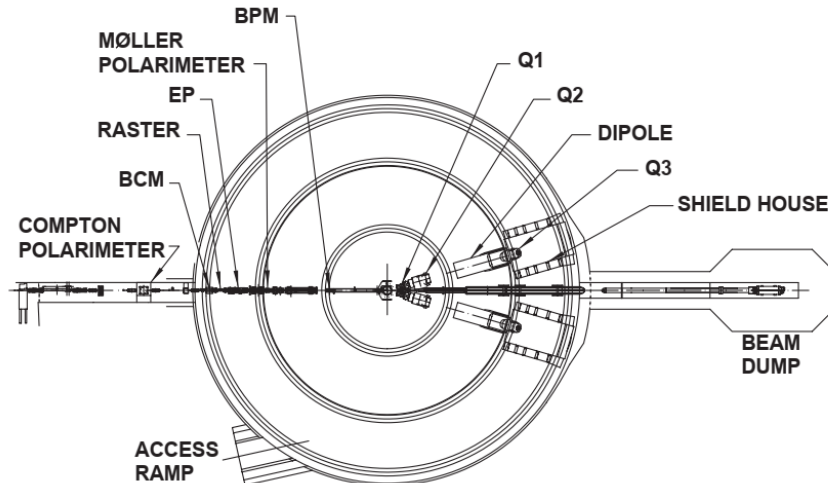
- Beam Position Monitor

Figure 8: An overhead schematic of Hall A.[30]

3.2.1 Arc Energy Measurement

Knowing the energy of the beam into the hall is critical for understanding the kinematics of the scattered electrons. This is done by measuring the deflection of the beam when passing through a

series of eight dipoles in the beam arc leading to the hall. This measurement requires wire scanners to measure the bend angle of the beam through the arc and a probe to measure the magnetic field integral of the dipole magnets.

The wire scanners are "harps" in the beamline, two before and two after the arc. A harp consists of three tungsten wires that are introduced sequentially into the path of the beam using a stepper motor. When the beam is incident on a wire, an electromagnetic shower is induced on the wire which is read by a PMT. By determining when each wire is struck by the beam, the position of the beam can be determined very accurately. Using two harps in each position also allows for beam direction measurement. Using a harp is a destructive measurement.
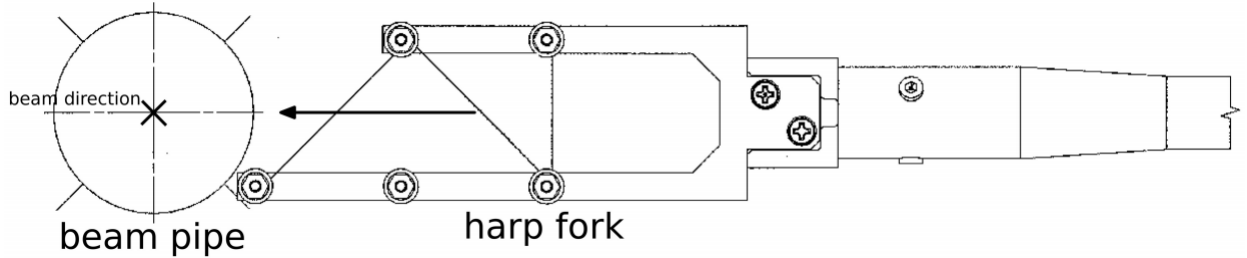

Figure 9: A schematic drawing of a harp scanner. The harp is introduced into the beamline with a stepper motor. The three wires create a signal when they interact with the beam, allowing for highly accurate beam position determination. The wires touching the beam is a destructive measurement.[31]

The field integral is measured on a ninth reference dipole that is not in the beamline. This ninth dipole is identical to the eight dipoles in the arc and is powered in series with the other dipoles. Measuring the field integral of the dipole requires a probe to be within the magnet, necessitating the use of this reference magnet.[32]

After measuring the field integral $\int \vec{B} \cdot \vec{dl}$ (in Tm) and angle θ (in radians), the momentum (in GeV/c) can be calculated with

$$p = k \frac{\int \vec{B} \cdot \vec{dl}}{\theta} \tag{3.1}$$

where $k = 0.299792$ GeV rad/(Tmc).

3.2.2 Beam Current Monitor

The Hall A Beam Current Monitor (BCM) is comprised of an Unser monitor and two RF cavities. The Unser, a Parametric Current Transformer, provides an absolute reference for the RF cavities.

22

The Unser is calibrated by putting a current on a wire that is inside of the Unser cavity and measuring the signal that is output. The calibration of the Unser drifts quite quickly, so it is used to calibrate the RF cavities but cannot be used for long-term monitoring.

Each RF cavity is tuned to the frequency of the beam (1.497 GHz). The resonance then produces a voltage proportional to the beam current. The signals are then split to be either sampled or integrated. The sampled signal outputs the RMS of the voltage over a 1 second period. This is equivalent to the average beam current for that second. The signal that is integrated is first sent to an RMS-to-DC converter which is then fed to a Voltage-to-Frequency converter. This signal is then sent to a scalar that accumulates over a run. The final scalar value is proportional to the total accumulated charge in the run.
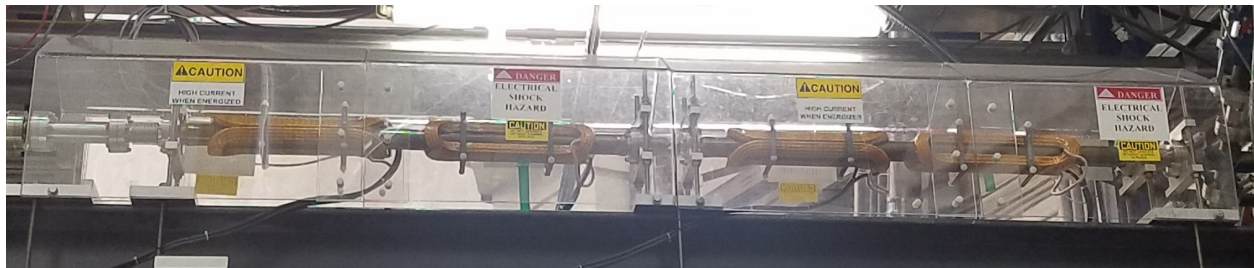
3.2.3 Raster

Figure 10: The Hall A raster consists of four dipole magnets on the beamline

When the beam enters Hall A it has very little spread, all of the electrons will strike the target in one small location (typically 80-200μm). This poses an issue for the targets in use. Depending on the beam current in use, a localized beam spot can significantly heat up the target. In the case of solid targets, this risks melting the target. For gas targets, there is a potential for cell rupture. The raster, shown in Figure 10, exists in the beamline to mitigate this risk by spreading the beam over a larger area on the target. The larger beam spread helps to reduce localized heating of the target due to the incident beam. The raster is a set of four dipole magnets: two for steering horizontally (x) and two for steering vertically (y).[33]

The magnet pairs that work in the same direction are synced, which ensures that they maximize the beam spread and do not work against each other. This characteristic can be seen in Figure 11. Each raster magnet is powered by a triangle wave of different frequencies to minimize harmonics.
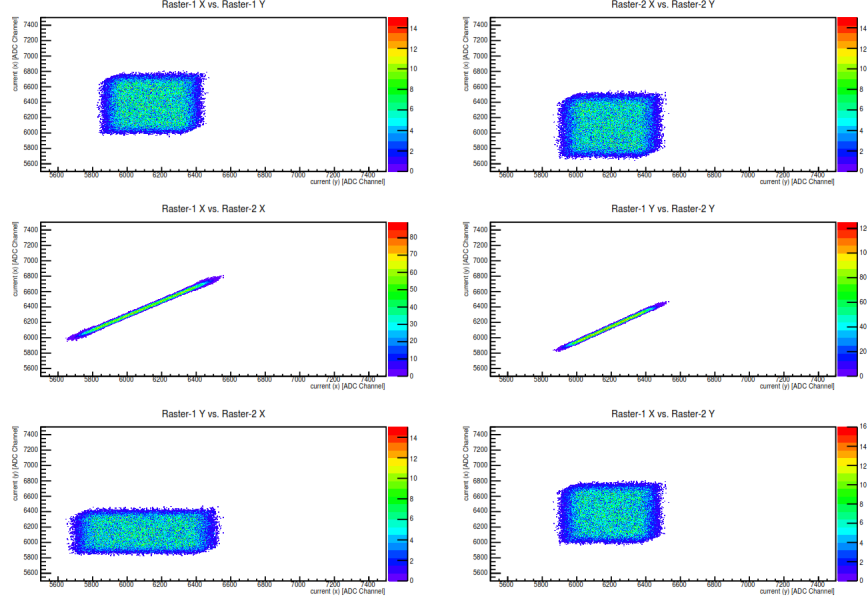
Figure 11: The X and Y raster pairs are each synced to produce the maximum kick. The X and Y directions are uncorrelated so that the beam travels uniformly over the target.
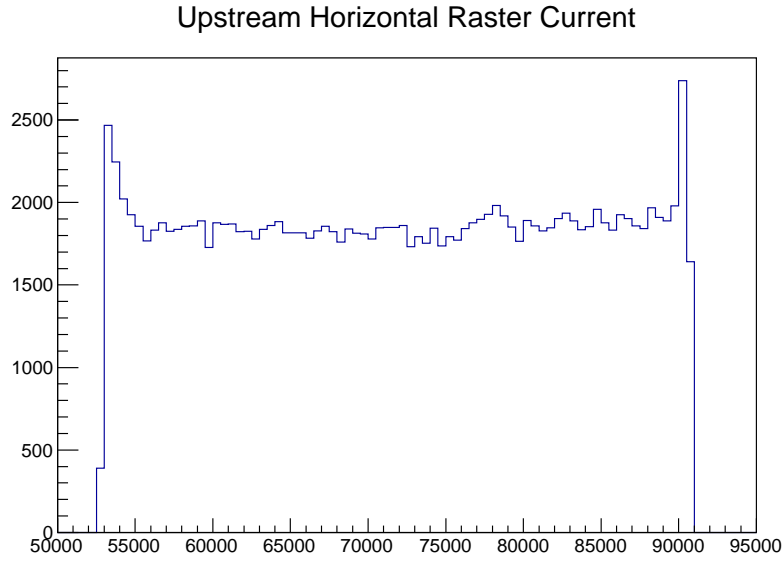
Figure 12: An example of a raster current spectrum. The range and size will change with ADCs used, beam energy, and raster size. The shape should always stay the same. The "bedposts" on the edges are due to rounding of the triangular waveform by a low-pass filter.

The horizontal rasters are set to 24.5 kHz and the vertical rasters are set to 25 kHz [34]. The triangle wave ensures that equal time is spent at all points in the rastered area. Figure 12 shows a

24

typical raster spectrum as recorded by the High Resolution Spectrometer (HRS).

3.2.4 Beam Position Monitors

The Beam Position Monitors (BPMs) are a pair of measurement devices that consist of four sensing wires. These four sensing wires are tuned to the fundamental frequency of the beam. Using the signal received from each wire, the experimenter can reconstruct the position of the beam as it passed the BPM. Using both BPMs in conjunction allows the experimenter to determine the beam trajectory and where the electrons are incident on the target. Using the BPMs alone provides only a reference position. The BPMs must be calibrated using a harp in order to measure the absolute beam position.
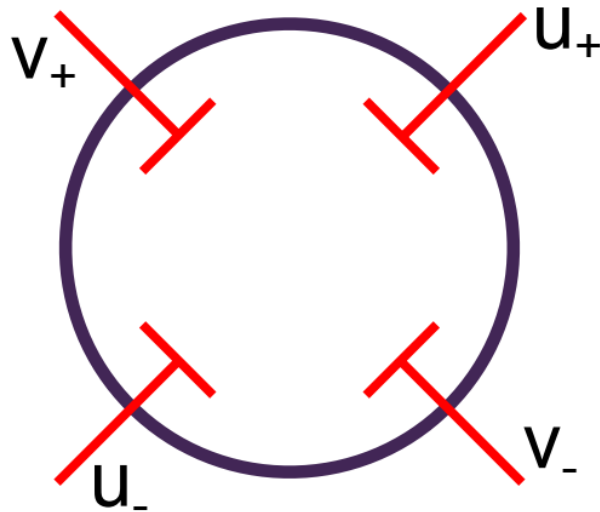
Figure 13: The BPM uses four sensing wires to determine the beam position. Since the wires do not actually touch the beam, this measurement can be done during data taking.[31]

The BPM electronics have a phase lag between the BPM measurement and the actual beam position. This means that the BPMs cannot provide position information on an event-by-event basis. However, they do provide a measure of the average position of the beam with a record of beam spread. This information, rather, is a critical component to calibrating the raster to provide accurate event-by-event position information.

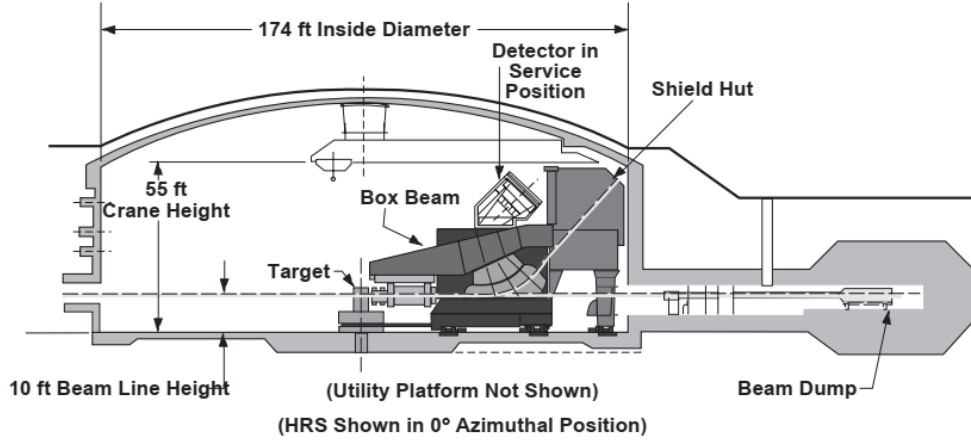Figure 14: A side-view schematic of Hall A showing the beamline, target, High Resolution Spectrometers, and Beam Dump. The beam will either interact with the target or pass through to the beam dump.[30]

3.3 Tritium Target System

When the beam reaches the center of Hall A, it will meet the target. Here the beam will either interact with the target and scatter, allowing for detection of events that are within the acceptance of the spectrometer, or pass through the target and be deposited in the beam dump. Figure 14 shows a side view of the hall, with the beam going from left to right. This view of the hall clearly shows these two possible paths for the beam (along the dashed line). For clarity, the spectrometer is drawn at a $0°$ scattering angle, which is not a position the spectrometer can physically occupy.

3.3.1 Gas Cell Design

The gas targets used in this experiment were housed in a specially designed cell. This cell deviates from typical cells used in Hall A in that the gas is not circulated. The need for such a design is to meet safety protocols when using a tritium target, specifically to minimize tritium material and to mitigate the risk of tritium leakage.

The target cells are 25 centimeters long and made of Aluminum 7075. The cells are sealed and utilize conductive cooling. The beam heating of the aluminum is approximately 11W. This heat is recovered by a copper heat sink that is actively cooled by 15K helium gas.[35] Figure 15 shows a 3-dimensional rendering of the target cell. The beam comes in from the bottom-left and passes through the center of the target along the length.
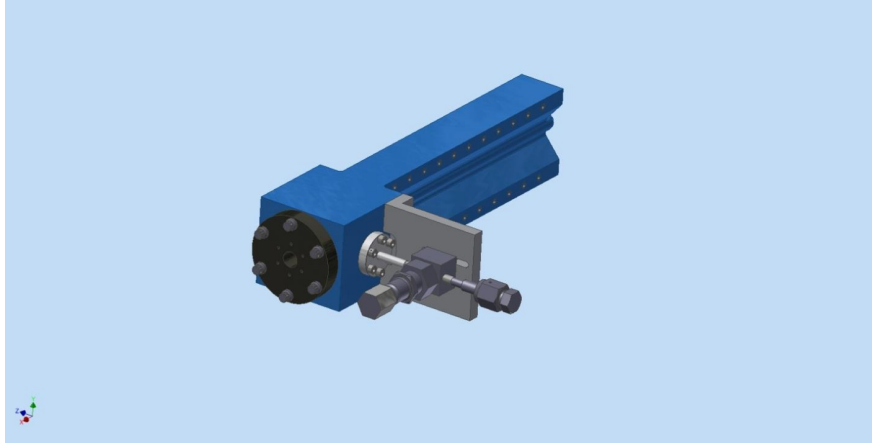
Figure 15: 3D rendering of the target cell. The black circular plate in the front is the upstream window of the cell.[35]

The lack of gas circulation allows for localized heating of the gas in the cell. This is caused by the energy being deposited into the gas by the incident beam. The heating causes a density change in the gas changing the effective target thickness. This characteristic must be addressed in the analysis of gas target data and is discussed in further detail in Section **??**.

3.3.2 Target Ladder

The MARATHON target ladder can be seen in Figure 3.3.2. This target ladder contained five targets that utilized the gas cell design described in the previous subsection. These are:

- Tritium

- Deuterium

- Hydrogen

- Helium-3

- Empty Cell

The cells that contain gas (i.e. all of the above except the empty target) are used for studying the physics goals of the MARATHON experiment. In particular, Helium-3 and Deuterium are the focus of this thesis. Table 2 lists the gas thicknesses and endcap thicknesses of the above gas targets.

Target	Gas Thickness g/cm²	Entrance Window Thickness (mm)	Exit Window Thickness (mm)
Tritium	77 ± 0.01	0.253 ± 0.004	$0.3430.047$
Deuterium	142.2 ± 0.8	0.215 ± 0.004	0.294 ± 0.056
Hydrogen	70.8 ± 0.4	0.311 ± 0.001	0.330 ± 0.063
Helium-3	53.4 ± 0.6	0.203 ± 0.007	0.328 ± 0.041
Empty cell	N/A	0.254 ± 0.0051	0.279 ± 0.0051

Table 2: Gas target thicknesses and cell wall thicknesses.[36]

In addition to the gas cells, the target ladder also contained several solid targets that are used for other studies. Those relevant to this thesis are:

- 25cm Dummy

- Carbon Hole - A carbon foil with a 2mm diameter hole in the center

- Raster Target - A "straw" for ensuring the beam is not coming in at an angle

The Empty target is a gas cell that has a vacuum inside. The 25cm Dummy is comprised of two Aluminum 7075 foils, this is the same material as the gas cells. The foils are spaced 25cm apart, the same length as the gas cells. Each foil is 0.3495 ± 0.0006 g/cm^2 thick, significantly thicker than the cell walls. These two targets are used to better understand the contribution of the gas cells to the electrons counted by the experiment. This study is discussed further in Section **??**.

The Carbon Hole target is a foil made of carbon that is 0.883 ± 0.0002 g/cm^2 thick with a $2mm$ diameter hole in the center. This target is used for centering the beam as well as for determining the settings needed for a $2mm$ by $2mm$ raster setting. This is also used to assist calibrating the raster as documented in Appendix **??**.

After the beam is centered and the raster settings are determined, the Raster Target is used. This target is a "straw" that the beam should pass straight through. The goal of using this is to ensure that the beam is not approaching the target at an angle. If any counts are seen above background, then the beam is hitting the straw and can be assumed to be coming in at an angle that needs to be rectified. If the beam is angled, electrons would leave the physics targets before passing through all of the target material. This would significantly reduce counting rates and make

Figure 16: The MARATHON target ladder.

it very difficult to determine the effective target thickness seen by the beam.

3.4 The Hall A High Resolution Spectrometer

Hall A has two 4 GeV/c High Resolution Spectrometers (HRSs), designated Left (LHRS) and Right (RHRS) corresponding to their orientation when looking downstream along the beam. In order to achieve Hall A's stated goal of 1% absolute cross section accuracy, the HRSs were designed to have 10^{-4} particle momentum resolution and 0.1 mrad in scattering angle resolution.

Each HRS has four superconducting magnets: three $\cos(2\theta)$ and a racetrack coil dipole. Utilizing a QQDQ magnet setup (named Q1, Q2, D, and Q3), each HRS has a 45° bending angle in a vertical bending plane. Each HRS has a similar, but unique, detector package that accommodates precise tracking and particle identification (PID). Figure 17 shows the magnet layout of the HRSs. The setup is identical on both the Left and Right HRS.

The two HRSs can be ran together for exclusive measurements or ran separately for inclusive measurements. MARATHON used each HRS separately in order to maximize counting rate. In
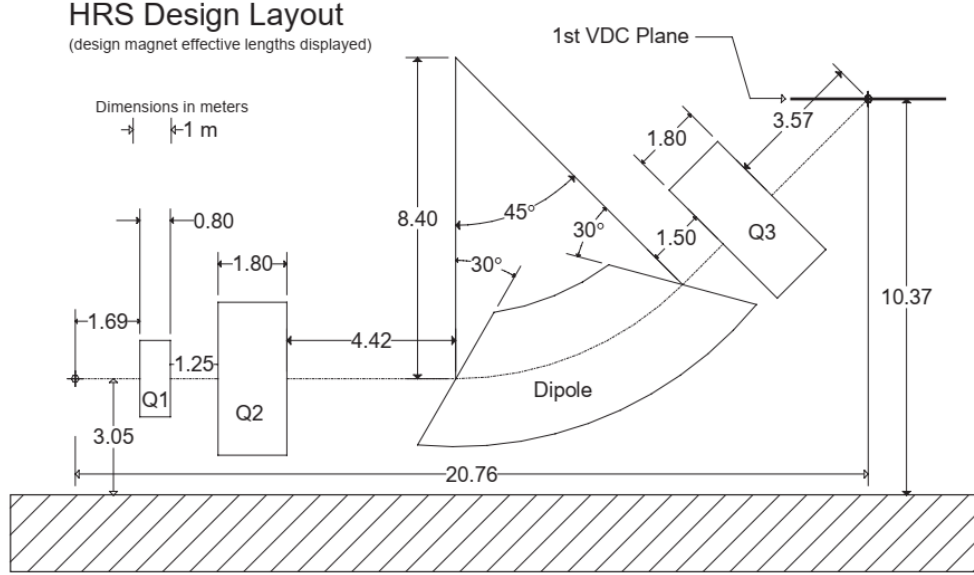
Figure 17: A schematic view of the HRS magnet setup. Particles enter from the left in Q1 and then pass through the magnets exiting Q3 into the first VDC plane.[30]

particular, the RHRS was parked at the highest angle measurement as the counting rate was very slow.

Each arm consists of a pair of Vertical Drift Chambers (VDCs), two scintillator planes, a gas cherenkov, and two leaded glass calorimeters. This combination of detectors allows for fine tracking and powerful electron identification.

3.4.1 Vertical Drift Chambers

Each arm has two VDCs at the entrance to the detector stack. These detectors are used for fine tracking of particles. Drift chambers are comprised of high voltage planes, sense wires, and a gas mixture. When a particle passes through a drift chamber it ionizes the gas. The high voltage planes keep a constant electric field within the drift chamber. The sense wires are held at ground potential. The ionized gas from incident particles then drifts toward the sense wire creating a build up of charge that can be measured. Using the drift speed of ions in the field and the time that it takes for the ion to reach the sense wire, the position of the track through the VDC can be accurately determined.

The chambers used in the HRSs, as seen in Figure 18, are oriented parallel to the horizontal plane of the hall and 45° to the detector stack. The active area of each VDC is 2118 mm by 288
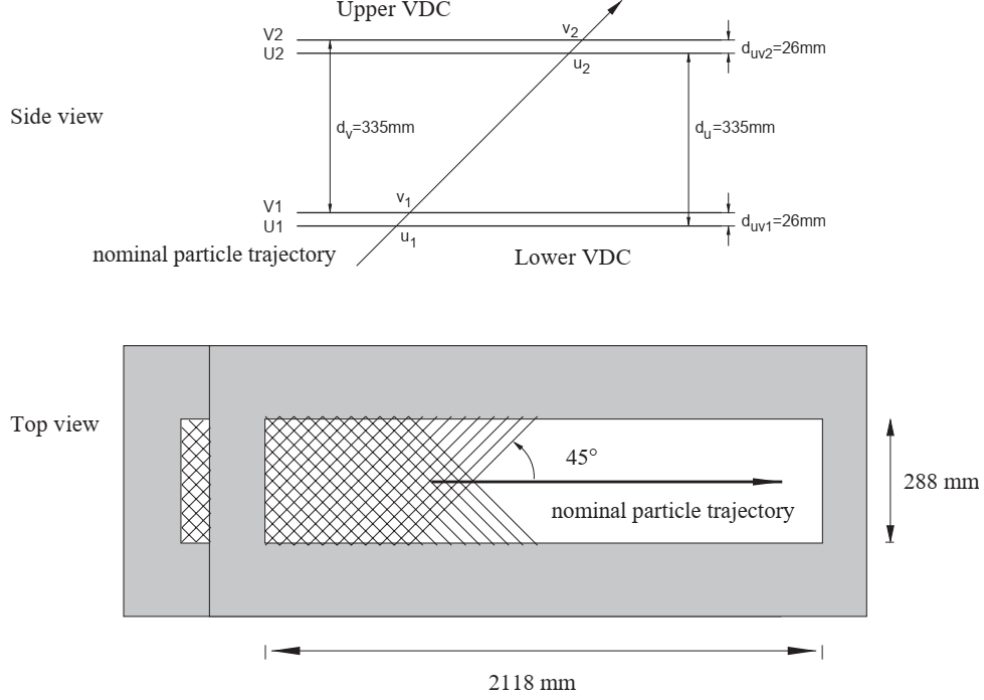
30

Figure 18: A schematic view of the VDCs. These are the first detectors in an HRS.[30]

mm. The gas used is an argon (62%) and ethane(38%) mixture. The electric field is created by gold-plated Mylar planes spaced 13 mm apart. These planes are held at -4 kV. Each chamber has two wire planes in a UV formation, that is 90° to each other, that are separated by 335 mm. In each plane there are 368 wires with a wire spacing of 4.24 mm. This setup gives a position resolution of 100 μm and an angular resolution of 0.5 mrad.

3.4.2 Scintillator Planes

Each HRS has two scintillator planes that were used for MARATHON: S0 and S2. These two planes sandwich the Gas Cherenkov. The scintillators are plastic paddles with a Photomultiplier Tube (PMT) on each end. When scintillating material is struck by a particle, it absorbs a small amount of energy and emits it as light. The light then travels through the material to the PMTs on each end. When the light reaches the PMT, it knocks electrons out of the photocathode. These electrons are accelerated through a series of exceedingly higher voltage dynodes where more electrons are released. Finally, this cascade reaches the anode with a enough electrons to create a signal that can be read in. This entire process is very quick, allowing the scintillators to be used for setting
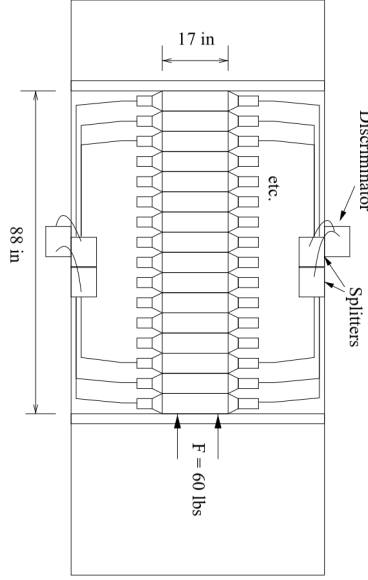
31

Figure 19: A schematic drawing of the S2 scintillator plane.[32]

the timing of events. The time difference between the signal in the PMTs on each end allows for rough tracking.

S0 consists of a single paddle with the PMTs on located on the top and bottom. The S0 paddle made from BICRON 408 scintillating plastic which is 10 mm thick, 170 cm long, and 25 cm wide. The PMTs used are $3''$ XP2312B. There is a trade-off in timing resolution when using a large paddle. The timing resolution of S0 is approximately $0.2ns$.

S2 consists of 16 paddles with the PMTs on the left and right. Each paddle is made from fast plastic scintillator EJ-230 and is 2 inches thick, 17 inches long, and 5.5 inches wide. The paddles are pressed together with a 60 pound force in order to minimize any space between the paddles. The PMTs used are $2''$ Photonis 2282B. Figure 19 shows the layout of the S2 scintillator plane. In this drawing, particles would pass through the plane of the page. The timing resolution of S2 has been measured to be smaller than $150ps$.

The signals measured in the scintillators form the basis for the HRS trigger. Since S2 has high time resolution, it serves to set the timing of the event. Proper event timing is critical for the VDCs to accurately track a particle.

3.4.3 Gas Cherenkov

The Gas Cherenkov is the first PID detector in the HRS. A gas cherenkov detector functions by observing cherenkov radiation from incident particles. Cherenkov radiation is light emitted by a particle that is traveling faster than the phase velocity of light in a medium. The cherenkov radiation is emitted as an "electromagnetic shock wave" in the wake of the particle that is then guided to PMTs by mirrors. This property allows a gas cherenkov detector to exclude low momentum particles.[37]

The Cherenkov chamber is filled with C02 at atmospheric pressure. This gas gives a 4.8 GeV/c momentum threshold for pion detection. This provides very efficient rejection of pions, as the HRSs have a momentum acceptance set much lower than that. Each chamber has ten spherical mirrors with focal length 80 cm each aimed at a PMT (Burle 8854). The radiator length is 80 cm for the LHRS and 130 cm for the RHRS.

All of these things means that analyzing the sum of all PMT signals allows for very efficient discernment between electrons and pions.

3.4.4 Leaded Glass Calorimeters

Both arms have two leaded glass calorimeters, known as the preshower and shower detectors. When a particle enters a calorimeter, it interacts with the material by depositing energy. This energy is converted into an electromagnetic shower of photons which are detected by PMTs attached to the glass blocks. How much energy is deposited is dependent on the particle and its radiation length within the material. In the case of the HRSs, the calorimeters are thick enough that electrons will completely deposit all of their energy into the preshower and shower detectors. Each HRS has a slightly different configuration for the calorimeters.

In the LHRS, the preshower and shower blocks are all perpendicular to the path of the particle. Both layers have are comprised of 34 blocks at alternate in size between 15 cm x 15 cm x 30 cm and 15 cm x 15 cm x 35 cm.

In the RHRS, the preshower blocks are perpendicular to the path of the particle while the shower blocks are parallel to the path of the particle. The preshower layer is composed of 48 blocks that measure 10 cm x 10 cm x 35 cm. The shower layer is composed of 80 blocks that measure 15 cm x 15 cm x 35 cm.
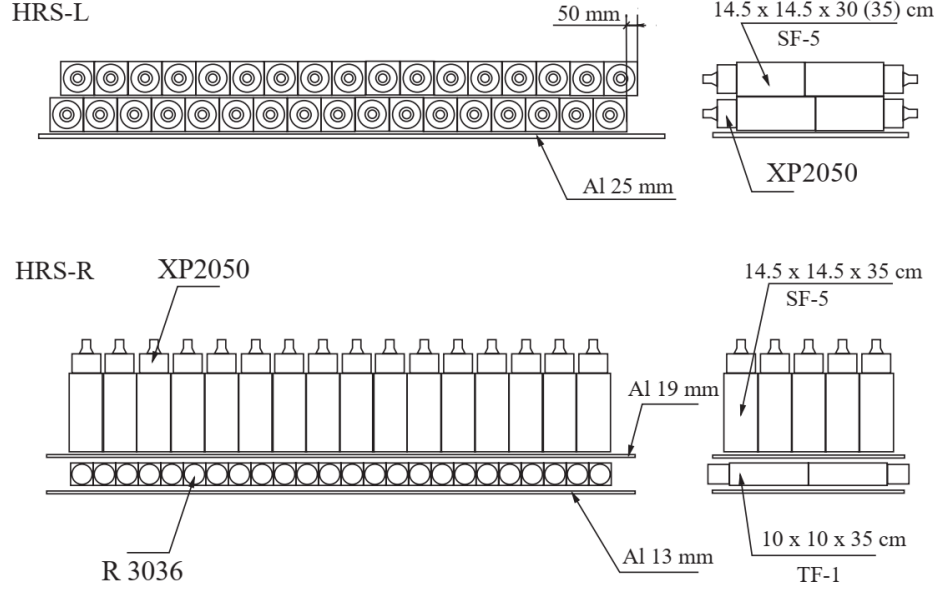
Figure 20: Layout of the shower blocks. Particles enter from the bottom of the page. Left is top-view. Right is side-view. [30]

The signal from the calorimeters is directly correlated to the energy of the particle that was detected. Typically for PID, a measure of E/p is used, that is the ratio of energy to momentum of the detected particle. This allows for very efficient identification of particles because electrons will peak around 1 and larger particles will have a much lower ratio.

3.4.5 Trigger

The HRSs read in data from the described detectors through a combination of Fastbus ADCs and TDCs and VME Flash ADCs. A Trigger Supervisor (TS) unit is used to distribute a trigger signal to this hardware. This trigger signals the ADCs and TDCs to record this signal and send it to be written. This process is overseen by CEBAF Online Data Acquisition (CODA) software written at JLab. The CODA software communicates with the TS crate to signal when it is ready to receive data and that triggers should begin being processed.

In order to distribute a signal to the ADCs and TDCs, the TS unit must receive an outside trigger. A trigger is a logic signal that is generated to indicate that the data that would be recorded is potentially a "good event". This trigger is generated from the signals that are produced by the detectors in the HRSs.

34

To produce this trigger, signals received from the scintillators and cherenkov are processed by NIM electronics. First, the signals are scintillator PMT signals are "discriminated". Each of these signals are then passed through a discriminator which, provided the signals are large enough to exceed a set threshold signifying a real signal, converts the signal into a logic pulse. The length of these logic pulses is set to allow for timing the coincidence of these three detectors. The PMTs in each scintillator plane are then checked for coincidence, that is any signal received within a designated window of time is defined as being from the same event. In the setup for S0, both PMTs must have a signal for this process to consider there to have been an event. The S2 setup requires that any single paddle must have a signal from both PMTs in order to trigger. For the cherenkov, the PMT signals are summed and then discriminated. The logic pulses for each detector are then delayed to allow for timing of coincidence between detectors. The need for delaying the signals is due to the varying length of cables from the detectors to the processing hardware.

These logic signals are finally combined into four different triggers:

- S0 || S2

- S0 && S2

- (S0 || S2) && Cherenkov

- (S0 && S2) && Cherenkov

Ultimately, the final three of these triggers were used in the experiment. A schematic of formation of these signals can be seen in Figure 21. In the formation of these triggers, the scintillators are used to set the timing for the TDCs. Particularly, S2 always sets the timing of the trigger since it has the highest timing resolution. In the case of the triggers where S0 and S2 are "OR'd", S0 will set the timing in the absence of an S2 signal.
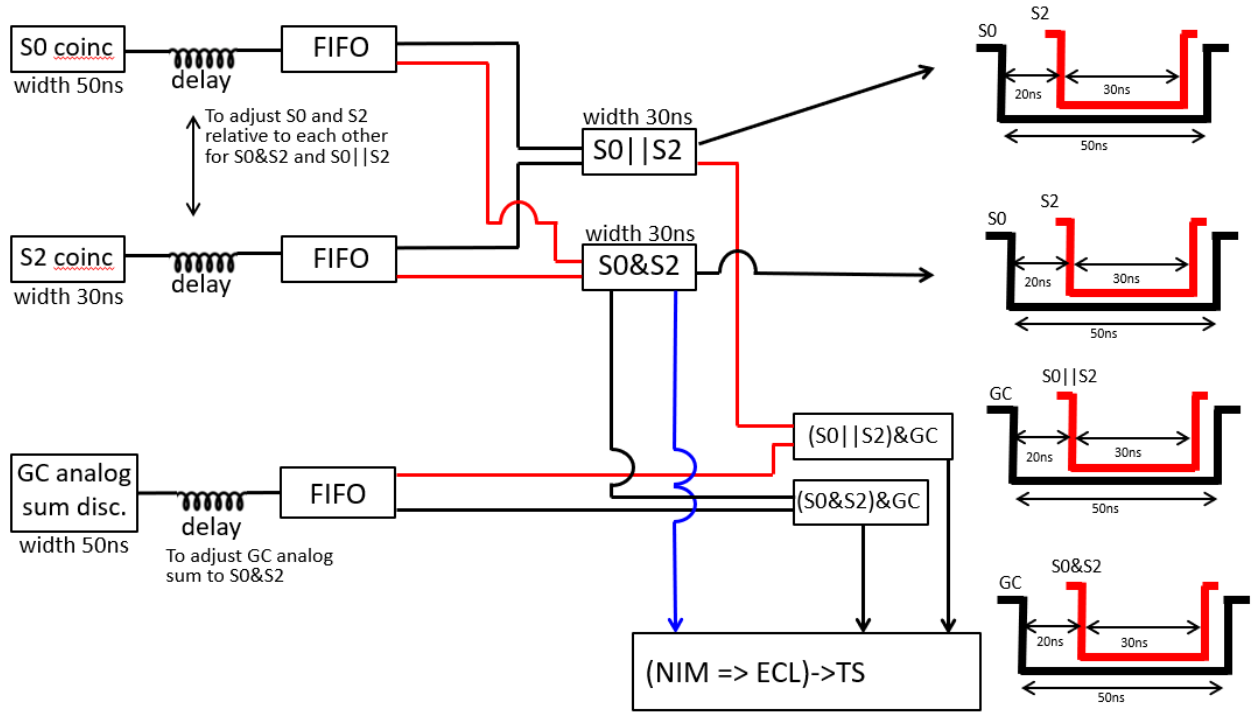
Figure 21: A schematic diagram of the trigger setup for MARATHON. In this diagram "disc." stands for discriminator. "FIFO" stands for "Fan in fan out", which is a unit that takes a signal and then outputs it to multiple channels. "NIM=>ECL" denotes the conversion from NIM to ECL logic standards which is necessary to interface with the Trigger Supervisor.[38]

Bibliography

[1]   D. Griffiths, *Introduction to Elementary Particles*, 2nd, WILEY-VCH, **2012**.

[2]   E. D. Bloom, D. H. Coward, et al., *Physical Review Letters* **1969**, *23*, 930–934.

[3]   E. M. Riordan, *Science* **1992**, *256*, 1287–1293.

[4]   E. M. Henley, A. Garcia, *Particles and Nuclei*, Springer, **2008**.

[5]   B. Povh, K. Rith, et al., *Particles and Nuclei: An Introduction to the Physical Concepts*, Second, Springer.

[6]   W. E. Burcham, M Jobes, *Nuclear and Particle Physics*, Longman Scientific & Technical.

[7]   J. D. Bjorken, *Physical Review* **1969**, DOI `10.1103/PhysRev.179.1547`.

[8]   A. Bodek, M. Breidenbach, et al., *Physical Review D* **1979**, DOI `10.1103/PhysRevD.20.1471`.

[9]   J. I. Friedman, H. W. Kendall, *Annual Review of Nuclear Science* **1972**, *22*, 203–254.

[10] D. Geesaman, K. Saito, et al., *Annual Review of Nuclear and Particle Science* **1995**, DOI `10.1146/annurev.nucl.45.1.337`.

[11] J. J. Aubert, G. Bassompierre, et al., *Physics Letters B* **1983**, *123*, 275–278.

[12] A. Bodek, N. Giokaris, et al., *Physical Review Letters* **1983**, *50*, 1431–1434.

[13] A. Bodek, N. Giokaris, et al., *Physical Review Letters* **1983**, DOI `10.1103/PhysRevLett.51.534`.

[14] P. R. Norton, *Rep. Prog. Phys.* **2003**, *66*, 1253–1297.

[15] R. G. Arnold, P. E. Bosted, et al., *Physical Review Letters* **1984**, DOI `10.1103/PhysRevLett.52.727`.

[16] J. Gomez, R. G. Arnold, et al., *Physical Review D* **1994**, *49*, 4348–4372.

[17] J. Ashman, B. Badelek, et al., *Physics Letters B* **1988**, DOI `10.1016/0370-2693(88)91872-2`.

[18] M. Arneodo, A. Arvidson, et al., *Nuclear Physics B* **1996**, *481*, 3–22.

[19] J Seely, A Daniel, et al., 1–5.

[20] G. Piller, W. Weise, *Physics Report* **2000**, *330*, 1–94.

[21] G. I. Smirnov, *European Physical Journal C* **1999**, *10*, 239–247.

[22] N. Armesto, *Journal of Physics G: Nuclear and Particle Physics* **2006**, *32*, DOI `10.1088/0954-3899/32/11/R01`.

[23] O. Hen, G. A. Miller, et al., *Reviews of Modern Physics* **2017**, *89*, DOI `10.1103/RevModPhys.89.045002`.

[24] A. Daniel, PhD thesis, **2007**.

[25] K. S. Egiyan, N. Dashyan, et al., **2003**, 1–11.

[26] L. B. Weinstein, E. Piasetzky, et al., *Nuclear Physics A* **2011**, *855*, 245–248.

[27] A. W. Thomas, *International Journal of Modern Physics E* **2018**, *27*, DOI `10.1142/S0218301318400013`.

[28] W. K. Brooks, H. Hakobyan, et al., **2014**.

[29] L. Cardman, R. Ent, et al., The Science Driving the 12 GeV Upgrade OF CEBAF, tech. rep., Jefferson Lab, **2001**.

[30] J. Alcorn, B. D. Anderson, et al., *Basic instrumentation for Hall A at Jefferson Lab, Vol. 522*, **2004**, pp. 294–346.

[31] P. Zhu, K. Allada, et al., *Nuclear Instruments and Methods in Physics Research Section A: Accelerators Spectrometers Detectors and Associated Equipment* **2016**, *808*, DOI `10.1016/j.nima.2015.10.086`.

[32] T. H. A. Collaboration, 2017 Version: Jefferson Lab Hall A Standard Equipment Manual, tech. rep., **2019**.

[33] R. Michaels, Private Communication.

[34] W. Gunning, Raster Frequency, **2017**.

[35] D. Meekins, Jefferson Lab Tritium Target Cell, tech. rep., **2014**.

[36]   D. Meekins, Hall A Tritium Target Configuration for December 2017, tech. rep. December 2017, JLab, **2018**, pp. 1–10.

[37]   W. R. Leo, *Techniques for nuclear and particle physics experiments A How-to Approach*, 2nd Revise, Springer-Verlag, **1994**.

[38]   R. Cruz-Torres, Private Communication.